**ISTANBUL TECHNICAL UNIVERSITY ★ INSTITUTE OF SCIENCE AND TECHNOLOGY**

# COMPUTATIONAL ANALYSIS OF HELICOPTER ROTOR FLOWFIELD IN HOVER AND FORWARD FLIGHT CONDITIONS

**M.Sc. Thesis by**
**Evren ÖNER, B.Sc.**

**Department :** **Advanced Technologies in Engineering**

**Programme:** **Aerospace Engineering**

**JUNE 2007**

**ISTANBUL TECHNICAL UNIVERSITY ★ INSTITUTE OF SCIENCE AND TECHNOLOGY**

# COMPUTATIONAL ANALYSIS OF HELICOPTER ROTOR FLOWFIELD IN HOVER AND FORWARD FLIGHT CONDITIONS

**M.Sc. Thesis by**
**Evren ÖNER, B.Sc.**

**(521041104)**

**Date of submission :** **17 July 2007**

**Date of defence examination:** **11 June 2007**

**Supervisor (Chairman):** **Prof. Dr. A. Rüstem ASLAN**

**Members of the Examining Committee** **Assoc. Prof. Dr. Fırat O. EDİS**

**Prof. Dr. Kadir KIRKKÖPRÜ**

**JUNE 2007**

İSTANBUL TEKNİK ÜNİVERSİTESİ ★ FEN BİLİMLERİ ENSTİTÜSÜ

# HELİKOPTER ROTORU ETRAFINDAKİ AKIŞIN ASKI VE İLERİ UÇUŞ DURUMLARINDA SAYISAL ANALİZİ

**YÜKSEK LİSANS TEZİ**
**Uzay Müh. Evren ÖNER**
**(521041104)**

**Tezin Enstitüye Verildiği Tarih : 17 Temmuz 2007**
**Tezin Savunulduğu Tarih : 11 Haziran 2007**

| | |
|---|---|
| **Tez Danışmanı :** | **Prof. Dr. A. Rüstem ASLAN** |
| **Diğer Jüri Üyeleri** | **Doç. Dr. Fırat O. EDİS** |
| | **Prof. Dr. Kadir KIRKKÖPRÜ** |

**HAZİRAN 2007**

## PREFACE

I would like to thank my advisor, Prof Dr. A. Rüstem ASLAN for his valuable support and understanding.

Special thanks to Kerem for his contributions and ideas. I would also like to thank to Ali, Hakan, Utku, Ersel, İlhan and Resul for their contributions and making the office (and out of the office) life more interesting.

Finally, I would like express my gratitude to my family for their continuous support through my entire life.

**June 2007** **Evren ÖNER**

# TABLE OF CONTENTS

## LIST OF TABLES

# LIST OF FIGURES

**Page**

# HELİKOPTER ROTORU ETRAFINDAKİ AKIŞIN ASKI VE İLERİ UÇUŞ DURUMLARINDA SAYISAL ANALİZİ

## ÖZET

Bu çalışmada, helikopter rotoru etrafındaki akış alanı askı ve ileri uçuş durumlarında sayısal olarak incelenmiştir. Hesaplamalı akışkanlar dinamiği hesaplamaları için ticari bir sonlu hacimler Navier-Stokes çözücüsü olan ANSYS CFX 10 kullanılmıştır. CFX çözücüsünün kabiliyetlerinin anlaşılması ve ileri uçuş analizleri için bir temel oluşturmak amacıyla, iki palalı izole durumdaki model bir rotor askı durumunda analiz edilmiştir. Sayısal ağ Gridgen v15 yazılımı ile oluşturulmuştur ve yapısal ve yapısal olmayan hacim elemanları içermektedir. Palalar çevresinde yapısal bir sayısal ağ kullanılırken, palalardan uzak kısımlarda yapısal olmayan sayısal ağ kullanılmıştır. Hesaplama hacmini küçük tutmak amacıyla askı hali sınır şartları kullanılmıştır. Hesaplamalar üç farklı uçuş durumu için gerçekleştirilmiş, elde edilen sayısal sonuçlar pala üzerindeki çeşitli noktalarda deney verisiyle karşılaştırılmıştır. Karşılaştırma sonucunda kullanılan yöntem doğrulanmış ve sonrasında iki palalı AH-1G rotoru ileri uçuş şartlarında analiz edilmiştir. İleri uçuş analizleri için oluşturulan sayısal ağ palalar etrafında yapısal, palalardan uzaklaştıkça yapısal olmayan elemanlardan oluşmaktadır. İleri uçuş şartları için askı hali sınır şartı uygun olmadığından, askı haline göre çok daha büyük bir hesaplama hacmi oluşturulmuştur. Palaların ileri uçuş sırasındaki kanat çırpma ve yunuslama hareketleri uçuş testinde ölçülen açılar kullanılarak modellenmiştir. Ölçülen çırpma ve yunuslama açıları ve o anki pala konumu ile palaların yeni konumları hesaplanmış ve sayısal ağ elemanları değişen pala konumlarına göre güncellenmiştir. Sayısal sonuçlar, deneysel veriler ve diğer bir sayısal çalışmanın sonuçları ile karşılaştırılmıştır.

# COMPUTATIONAL ANALYSIS OF HELICOPTER ROTOR FLOWFIELD IN HOVER AND FORWARD FLIGHT CONDITIONS

## SUMMARY

In the present study, the flowfield around the helicopter rotors in hover and forward flight conditions are studied numerically using commercially available computational fluid dynamics (CFD) software, ANSYS CFX 10. Hover flight conditions for a two-bladed isolated rigid rotor was analyzed for assessing the capabilities of the solver and to form a basis for forward flight analyses. Computational grid generation was carried out using Gridgen v15 software. Structured grid elements were used near the blade region while unstructured elements were used in the outer regions of the domain. Hover boundary conditions were utilized to keep the computational domain small. The computations are carried out for three different conditions and the results are compared with the experimental data for validation. Having validated the hover methodology, two-bladed AH-1G helicopter rotor was analyzed in forward flight conditions. Computational grid consists of structured elements near the blades and unstructured elements at the outer region. Blades' first harmonics, measured in the flight tests were used to prescribe the flapping and pitching motion of the blade. Using the first harmonics angles, new blade positions were calculated for the current azimuth angle and the computational mesh was updated accordingly. Comparisons with the flight test data and another numerical simulation were given at different stations for different azimuth angles.

# 1 INTRODUCTION

Helicopters have come a long way both in design and technology since the flight of the first helicopter. Today, they are indispensable for many civilian and military applications. Although the many problems encountered through the history of the helicopter design were solved, there is still need for research on topics such as improvement of performance and handling qualities, and reducing the noise-emission. All of those topics are deeply related to the flowfield around the helicopter, thus an efficient method for correctly predicting the flowfield around the helicopter is very important.

## 1.1 Helicopter Aerodynamics

A helicopter is an aircraft which is lifted and propelled by one or more horizontal rotors consisting of two or more rotor blades. The rotor of a helicopter provides vertical lifting force equal in magnitude to the helicopter weight, a propulsive force needed to overcome vehicle drag in forward flight and means of generating forces and moments needed to control the altitude and position of the helicopter.[1] There are four flight regimes in which the helicopter operates. First is hover, in which the thrust generated by the rotor blades is equal to the weight of the helicopter, and the helicopter remains stationary above the ground. The second flight regime is vertical climb, in which additional thrust is required to move the helicopter upward. Third is the vertical descent and the final one is the condition of forward flight, in which the rotor disk is tilted in the direction of the flight to create a thrust component to overcome the vehicle drag [2].

The ideal situation for a helicopter is the generation of a constant lift by the rotor blades throughout the rotor cycle. The lifting capability of a rotating helicopter blade is related to its local angle of attack and local dynamic pressure. The blade position is defined in terms of an azimuth angle, $\psi$, which is zero when the blade is pointing downstream. In hover, the velocity variation along the blade is azimuthally axisymmetric and radially linear, zero at the hub and maximum, $V_{tip}$, at the blade tip.

In forward flight, free stream velocity, $V_{\infty}$, add to or subtracts from the rotational velocity at each part of the blade and while the velocity distribution is still linear, it varies in magnitude with respect to the blade azimuth angle (Figure 1.1). As the rotor blade moves in the same direction as the forward flight speed ($\psi$=180, advancing side), $V_{tip}$ is large enough to provide sufficient lift but as the blade moves in the opposite direction of flight ($\psi$=0, retreating side), relative velocity is smaller and local angle of attack must be larger to achieve the same total lift. This inequality in the lift distribution creates rolling moments which must be balanced with trimming the rotor, that is, the angle of attack of the blades on the advancing and retreating sides must be adjusted periodically with respect to the azimuth angle. This periodic adjustment of angle of attack is called cyclic pitch. If the each of the blades' angle of attack is increased simultaneously to achieve a higher lift, it is called the collective pitch [2].

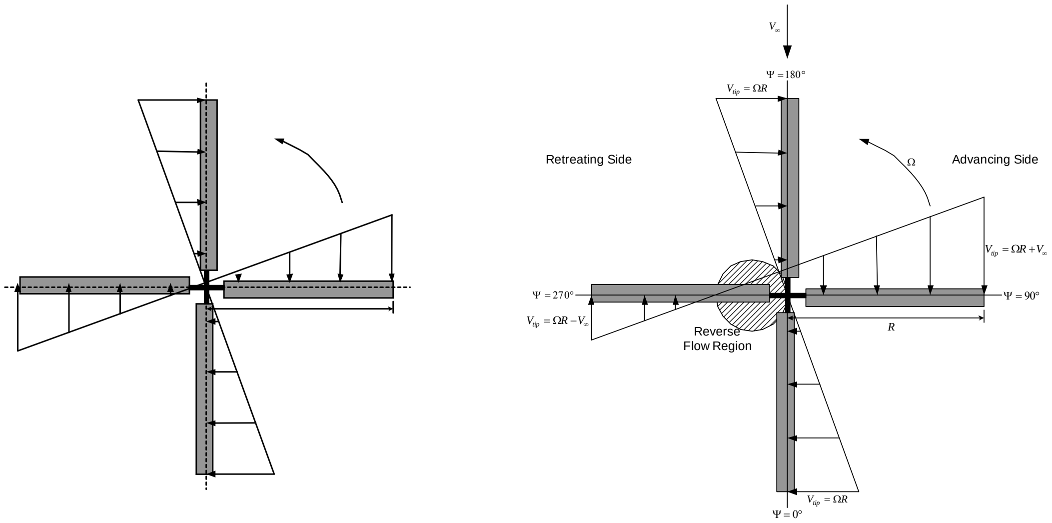

**Figure 1.1:** Velocity distributions along the blades during hover and forward flight [1]

Helicopter rotors are often hinged to provide trim capability and to minimize the effects of aeroelastic stresses, that is, the rotor blades are permitted to bend out of the rotor disk plane and pitch to satisfy trim requirements. As can be seen from the Figure 1.2, there are two types of hinges possible: lead-lag hinge which permits the motion of the blade within the rotor-disk plane and the flapping hinge permitting the flapping motion of the blades out of the rotor-disk plane. A rotor having both hinges is said to be a fully articulated rotor but it is also possible to have a hingeless rotor by using aeroelastically soft blades, thus keeping the hub stresses close to minimum.

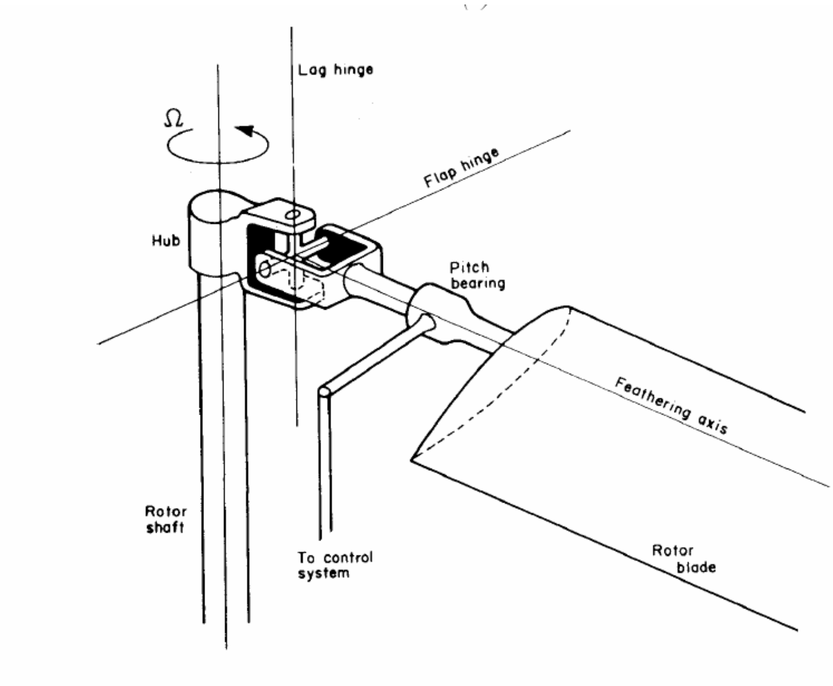

**Figure 1.2**: Lead-lag and flapping hinges [2]

The complexity of the flow induced by a helicopter can be appreciated from Figure 1.3. The flow field in which the rotor operates is considerably more complex than of a fixed-wing aircraft. Unlike on a fixed wing, due to the rotational speed of the blades, high dynamic pressure found at the tips of a helicopter blade produces strong tip vortices and these tip vortices remain close to the rotor and to the following blades for several rotor revolutions [1]. Moreover, as the blades rotate, the tip vortex shed from one of the blades may collide with a following blade and so called blade vortex interactions (BVI) occur. Besides affecting the rotor performance, BVI is a major source of the rotor noise of the helicopter. There are also interactions between the main rotor-fuselage and main rotor-tail rotor because of this wake structure. Another complexity comes from the inherently asymmetric nature of the flow over the rotor disk. The flow may be transonic or locally supersonic on the advancing side near the tip and shock waves will likely be present. On the retreating blade side, because of the trim requirements, the angle of attack is large and the flow may be stalled if these angles become too large. This results in a loss of overall lifting and propulsive capability from the rotor. Because of the inherent time-dependent nature of the flow around the rotor blades in forward flight, retreating blade stall is highly unsteady and is referred to as dynamic stall [2].

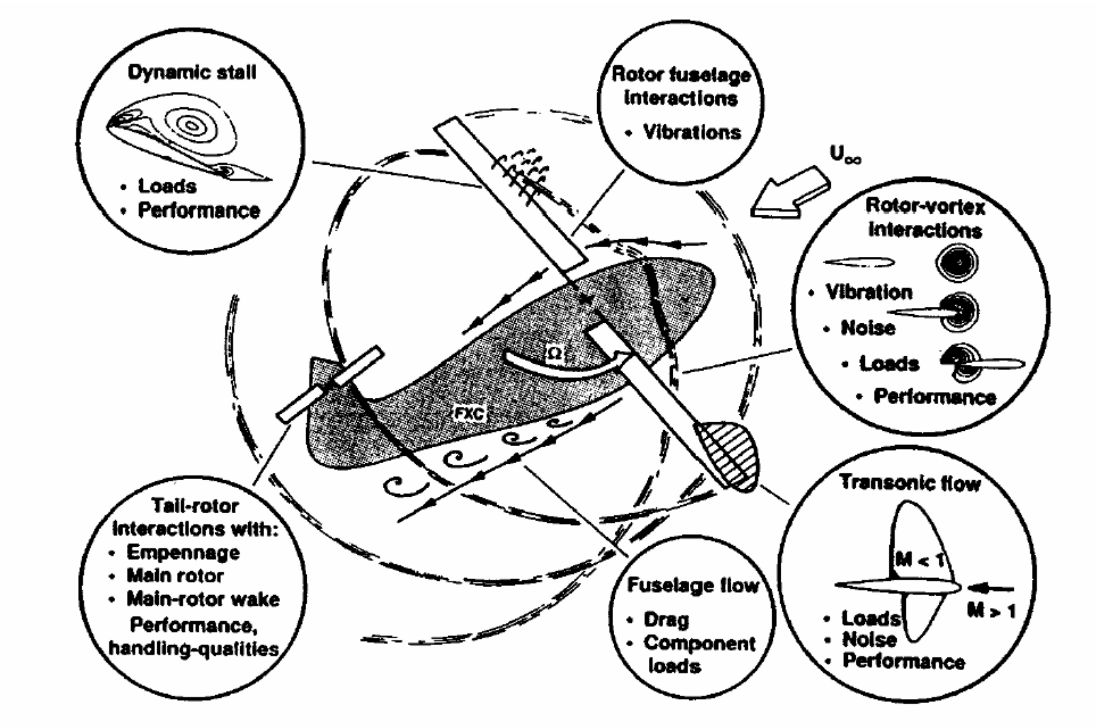

**Figure 1.3:** A summary of specific flow problems which occur on a helicopter [3]

The computation of the helicopter flowfield, especially in forward flight, requires accurate and efficient modeling of the problems mentioned above. In order to capture the physical phenomena, the influence of the inflow, blade dynamics, elastic response and the trim of the rotor must all be properly included in any Computational Fluid Dynamics (CFD) analysis. But the existing CFD tools are not yet able to simulate the entire range of physical phenomena so some of the influences are either ignored or computed externally to the CFD calculations.

## 1.2 Simulation Methodologies

The simplest method of analyzing rotor wings uses simple momentum theory and blade element theory. Both of these methods were formed by drawing an analogy to the ship propellers and then applying these studies to rotorcraft. These methods formed the basis of the design of helicopters up through the 1960s and still provide a basis for assessing the basic helicopter performance today [2].

With the advent of high speed computers, researchers began to use CFD techniques. Computational studies for calculating the rotor flowfield in hover and forward flight has started with the solution of the transonic small-disturbance equation and progressed to the solution of the full-potential equation when computers became powerful enough to model helicopter aerodynamics using finite difference potential flow methods in the early 1980s [4]. Egolf and Sparks [5] solved the full potential equation using a rotary wing extension of an existing fixed-wing code. They couple this solution with a prescribed wake method in which the vortex system is defined using a vortex lattice method. Strawn and Caradonna [6] solved a conservative unsteady full potential equation with a modified fixed-wing code and produced results for a symmetric airfoiled, untwisted, untapered blade. Steinhoff and Ramachandran [7] tried to overcome the false diffusion of vorticity due to the grid sizes, by embedding the vortex structure into the flow and calculate the vortical flow itself. Ramachandran et al. [8] solved the full-potential equation on an adaptive grid, and incorporated blade motion.

In contrast to vortex and full potential formulations, the Navier-Stokes equations contain the physics for vorticity generation at a surface and subsequent convection into the wake, thus capture the rotor wake as a part of the solution. Wake and Sankar [9] were the first to present solutions to the unsteady Navier-Stokes equations for a rigid rotor blade. They used a C-grid and an implicit time marching algorithm based on a Beam and Warming scheme. Srinivasan et. al. [10] modeled the influence of the far-field boundary conditions used in Navier-Stokes computations of a hovering rotor with a three-dimensional sink to satisfy mass flow requirements. Srinivasan and Baeder [11] have produced solutions for a forward flight condition with the flow being locally supersonic near the blade tips. Ahmad and Duque [12] used moving embedded grids in their calculation for the rotor system of the AH-1G helicopter in forward flight conditions. They modeled both pitching and flapping motions of the blades and partially trimmed the rotor externally. Steijl et. al. [13] used mesh deformation for modeling the blade motions and coupled their Navier-Stokes solver with a trimming code and produced results for hovering and forward flying rotors. Pomin and Wagner [14] used moving embedded grids and coupled their CFD solver with a finite element model of the blades instead of prescribing the flapping and pitching motion.

### 1.3 Research Objective and Scope

Although modern Navier-Stokes codes still may not surpass the accuracy of global performance prediction and qualitative results of the comprehensive analysis methods that are being used for industrial design, such as blade element theory, due to the limitations in computing resources and numerical diffusion problems of the rotor wake, they can provide valuable insight into the three-dimensional flowfield [14].

In the present study, the flowfield around the helicopter rotors in hover and forward flight conditions are studied numerically using commercially available CFD software [15], to develop a solution methodology that will accurately predict the aerodynamic loads on the rotors. Hover flight conditions for an isolated rigid rotor was analyzed for assessing the capabilities of the solver and to form a basis for forward flight analyses. The computations are carried out for various flow conditions with different tip Mach numbers and collective pitch settings and the results are compared with the experimental data of Caradonna & Tung [16] for validation. Having validated the hover methodology, AH-1G rotor [17] was analyzed in forward flight conditions. Blades' first harmonics, measured in the flight tests are used to prescribe the blade motion. Comparisons with experiments [17] and other numerical simulations [4] were given.

For the hovering rotor analyses, validation was made against the experimental study of Caradonna & Tung [16]. In that experiment, an untwisted, rectangular planform, 6:1 aspect ratio blades with NACA 0012 airfoil were used. Structured-unstructured hybrid grids were produced using commercial grid generation software. Shear Stress Transport (SST) turbulence model was used to account for the turbulence effects. The boundary conditions obtained from one dimensional momentum theory by Sirinivasan et. al. [10], required for the rotor analysis is externally fed in to the Navier-Stokes solver to simulate proximity flow conditions about a rotating rotor.

The rotor used for forward flight validation was an AH-1G two bladed rotor [17]. Blades have a $10^0$ twist with a rectangular planform. Structured-unstructured hybrid grids were generated using commercial grid generation software. Shear Stress Transport (SST) turbulence model was used to account for the turbulence effects. Farfield boundary conditions were applied at the boundaries. Rigid blade motion was assumed and blade motion was modeled using blades' first harmonics measured in the flight tests. A trimmed rotor configuration was used in the calculations and no other trimming was made. The computations were performed on a SGI Altix 3000 high performance computing system.

The rest of this thesis is structured as follows: In the second chapter, the mathematical and numerical formulation is given. Detailed information on initial and boundary conditions is given in chapter 3. In Chapter 4, implementation details and the details of the hover and forward flight cases are given. Results are presented along with the discussions in chapter 5. Conclusions are given in chapter 6.

# 2 MATHEMATICAL AND NUMERICAL FORMULATION

The governing equations for hovering and forward flying rotors are the Navier-Stokes equations. Additional terms are added to the N-S equations if they are solved in a rotating reference frame. Calculations are performed using a commercial Navier-Stokes solver, ANSYS CFX 10.

The governing equations employed by the CFX solver, boundary condition formulation for the hovering rotor and the prescribed flapping and pitching motion equations employed for the forward flying rotor are explained below.

## 2.1 Governing Equations

### 2.1.1 Continuity Equation

Continuity equation in the general form, which is valid for incompressible and compressible flows, is given as follows:

$$\frac{\partial \rho}{\partial t} + \nabla \bullet \left( \rho \mathbf{U} \right) = 0 \tag{2.1}$$

where $\rho$ the density and **U** is the velocity vector.

### 2.1.2 Momentum Equation

Conservation of momentum is defined as:

$$\frac{\partial \rho \mathbf{U}}{\partial t} + \nabla \bullet \left( \rho \mathbf{U} \otimes \mathbf{U} \right) = \nabla \bullet \left( -p\delta + \mu \left( \nabla \mathbf{U} + \left( \nabla \mathbf{U} \right)^T \right) \right) + S_M \tag{2.2}$$

where p is the static pressure, $\delta$ is the Kronecker delta function, $\mu$ is the dynamic viscosity. $S_M$ denotes the additional momentum sources.

### 2.1.3 Energy Equation

$$\frac{\partial \rho h_{tot}}{\partial t} - \frac{\partial p}{\partial t} + \nabla \bullet \left( \rho \mathbf{U} h_{tot} \right) = \nabla \bullet \left( \lambda \nabla \mathrm{T} \right) + S_E \tag{2.3}$$

where T is the temperature, $\lambda$ is the thermal conductivity, $h_{tot}$ is total enthalpy and $S_E$ denotes additional energy sources. $h_{tot}$ is given in terms of static enthalpy as:

$$h_{tot} = h + \frac{1}{2} U^2 \tag{2.4}$$

where

$$h = h\left( p, \mathrm{T} \right) \tag{2.5}$$

If the viscous forces are dominant in the flow, then the energy equation becomes:

$$\frac{\partial \rho h_{tot}}{\partial t} - \frac{\partial p}{\partial t} + \nabla \bullet \left( \rho \mathbf{U} h_{tot} \right) = \nabla \bullet \left( \lambda \nabla \mathrm{T} \right) + \nabla \bullet \left( \mu \nabla \mathbf{U} + \nabla \mathbf{U}^T - \frac{2}{3} \nabla \bullet \mathbf{U} \delta \mathbf{U} \right) + S_E \tag{2.6}$$

## 2.2 Rotating Reference Frame

Flows around rotating equipment can be modeled using a rotating reference frame. In this situation, the coordinate system is moved with the rotating equipment and experiences a constant acceleration in the radial direction. Since the rotating boundaries move at the same speed as the reference frame, they become stationary relative to the rotating frame.

For flows in a rotating frame of reference, rotating at a constant angular velocity $\omega$, additional sources of momentum are required to account for the effects of the Coriolis force and, in compressible flow, the centrifugal force:

$$S_{M,rot} = S_{Cor} + S_{cfg} \tag{2.7}$$

where

$$S_{cfg} = -\rho\omega \times (\omega \times r) \tag{2.8}$$

$$S_{Cor} = -2\rho\omega \times U \tag{2.9}$$

And where r is the location vector and U is the relative frame velocity. In the energy equation, the advection of total enthalpy is replaced by the advection of rothalpy which is given by:

$$\mathrm{I} = h_{stat} + \frac{1}{2}U^2 - \frac{1}{2}\omega^2 R^2 \tag{2.10}$$

Since the rotation energy is not included in the transient term in the energy equation, rotational enthalpy is only conserved in the transient solution if $\omega$ is constant [15].

## 2.3 Turbulence Modeling

ANSYS CFX software offers a wide range of turbulence models, from the standard $k-\varepsilon$ model to large eddy simulation (LES). Most turbulent flow calculations use the standard $k-\varepsilon$ model because of its economy and reasonable accuracy for a wide range of flows. However, the model tends to predict the onset of separation too late as well as to under predict the amount of separation. Predicting the reduced separation is necessary in forward flight calculations because of the possibility of the dynamic stall. Shear stress transport (SST) model has been developed to solve this problem [18]. SST model works by solving a turbulence/frequency-based model ($k-\omega$) at the wall and $k-\varepsilon$ in the bulk flow. A blending function ensures a smooth transition between the two models.

This study uses SST for the turbulence modeling both for the hover and forward flight calculations.

### 2.3.1 Shear Stress Transport (SST) Model

SST model is a $k-\omega$ based model that accounts for the transport of the turbulent shear stress and gives highly accurate predictions of the onset and the amount of flow separation under adverse pressure gradients [15, 18].

Proper transport behavior can be obtained by adding a limiter to the formulation of the kinematic eddy-viscosity:

$$v_t = \frac{a_1 k}{\max\left(a_1\omega, SF_2\right)} \tag{2.11}$$

where

$$v_t = \mu_t / \rho \tag{2.12}$$

S is an invariant measure of the strain rate. F2 is a blending function which restricts the limiter to the wall boundary layer, as the underlying assumptions are not correct for free shear flows. The blending functions are critical to the success of the method. Their formulation is based on the distance to the nearest surface and on the flow variables.

$$F_1 = \tanh\left(\arg_1^4\right) \tag{2.13}$$

with:

$$\arg_1 = \min\left(\max\left(\frac{\sqrt{k}}{\beta' \omega y}, \frac{500\,v}{y^2 \omega}\right), \frac{4\rho k}{CD_{kw}\sigma_{\omega 2} y^2}\right) \tag{2.14}$$

where y is the distance to the nearest wall and v is the kinematic viscosity and:

$$CD_{k\omega} = \max\left(2\rho \frac{1}{\sigma_{\omega 2}\omega} \nabla k \nabla \omega, 1.0\times 10^{-10}\right) \tag{2.15}$$

$$F_2 = \tanh\left(\arg_2^2\right) \tag{2.16}$$

with:

$$\arg_2 = \max\left(\frac{2\sqrt{k}}{\beta' \omega y}, \frac{500 v}{y^2 \omega}\right) \tag{2.17}$$

Closure coefficients are given as:

$$\begin{aligned}
&\beta' = 0.09 \\
&\alpha_1 = 5/9 \\
&\beta_1 = 0.075 \\
&\sigma_{k1} = 2 \\
&\sigma_{\omega 1} = 2 \\
&\alpha_2 = 0.44 \\
&\beta_2 = 0.0828 \\
&\sigma_{k2} = 1 \\
&\sigma_{\omega 2} = 1/0.856
\end{aligned} \tag{2.18}$$

## 2.4 Hover Boundary Condition

Determinations of appropriate boundary conditions are very important to obtain realistic behavior in the wake of a hovering rotor. Although the rotor wake is rapidly swept away from the rotor in forward flight, and out of the computational domain, the wake system remains close to the rotor blades for a number of rotor revolutions in hover position.  Because of this, definition of appropriate far-field boundary conditions is much more important in hover position. The method described by Srinivasan et al. [10] to determine inflow/outflow boundary conditions for the hovering rotor uses helicopter momentum theory to approximate the boundary conditions. Using this theory, far field outflow velocity due to the rotor wake system can be related to the thrust from the rotor blade by:

$$W_e = -2M_t\sqrt{\frac{C_t}{2}} \tag{2.19}$$

where

$$C_T = \frac{T}{\rho(\pi R^2)(\Omega R)^2} \tag{2.20}$$

$$M_{tip} = \frac{\Omega R}{a_\infty} \tag{2.21}$$

T is the thrust, R is the rotor radius, Ω is the rotor radial speed, a is the speed of sound, ρ is the density of air and V is the velocity magnitude.

This velocity is uniform and occurs below the rotor blade over an exit area equal to one half of the area of the rotor disk which can be seen Figure 2.1.

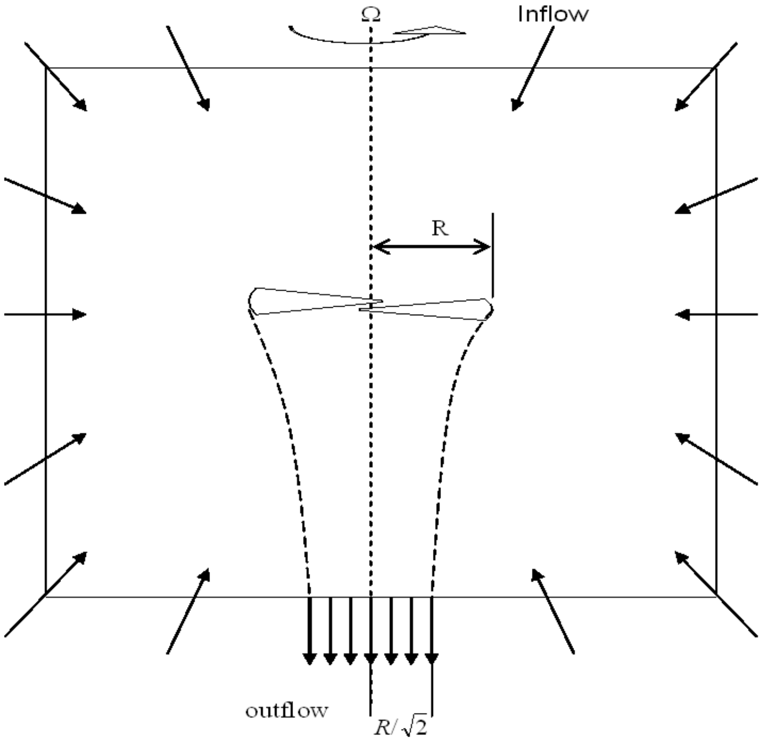

**Figure 2.1:** Boundary conditions for the hovering rotor

In order to satisfy continuity through out the domain, inflow velocities are prescribed by:

$$W_r = -\frac{M_t}{4}\sqrt{\frac{C_t}{2}}\left(\frac{R}{r}\right)^2 \tag{2.22}$$

Using above formulation, a user defined expression was defined to apply inflow velocities at the boundary faces. A user defined expression is used for defining new variables, thus enhancing the standard features of the CFX solver. It is possible to access all of the flow variables and derive new variables from them using a user defined expression.

## 2.5 Domain Interfaces

Domain interfaces provide a way of connecting meshes or computational domains together. In forward flight calculations Fluid-Fluid domain interfaces were used to model the change in reference frames between domains.

ANSYS CFX uses a control surface approach to perform the interface connection. A physically based intersection algorithm is employed to provide the means of changing the grid topology and physical distribution across the interface. This means that a domain interface can be successfully defined even when the surfaces on either side of an interface do not physically “fit” together to form a well defined physical connection. The treatment of the interface fluxes is fully implicit and fully conservative in mass, momentum, energy, scalars, etc. This means that the multigrid solver can be applied directly, without any penalty in terms of robustness or convergence rate [15].

## 2.6 Blade Motion

In the forward flight analyses, rigid blade motion was assumed and the periodic blade motion for pitch and flap as a function of blade azimuth was approximated using Fourier series [19].

*Pitch*

$$\theta = \theta_0 + \theta_{1c}\cos\psi(t) + \theta_{1s}\sin\psi(t) + \theta_{2c}\cos 2\psi(t) + \theta_{2s}\sin 2\psi(t) + \ldots \qquad (2.23)$$

*Flap*

$$\beta = \beta_0 + \beta_{1c}\cos\psi(t) + \beta_{1s}\sin\psi(t) + \beta_{2c}\cos 2\psi(t) + \beta_{2s}\sin 2\psi(t) + \ldots \qquad (2.24)$$

$$\psi(t) = \Omega t \qquad (2.25)$$

Eulerian angles were used to prescribe the motion of the blades. At each time step, blade rotates by an increment of azimuth ($\psi$) that results in a change in pitch ($\theta$)

and flap ($\beta$). Starting with the initial position, the change in the blade position can be evaluated using the well-known transformation [12]:

$$\vec{x}_{new} = T\vec{x}_{old} \tag{2.26}$$

Where transformation matrix T is given in the terms of the Eulerian angles as

$$T = \begin{bmatrix} t_{11} & t_{12} & t_{13} \\ t_{21} & t_{22} & t_{23} \\ t_{31} & t_{32} & t_{33} \end{bmatrix} \tag{2.27}$$

$$\begin{aligned}
t_{11} &= \sin\psi\cos\theta + \cos\psi\sin\theta\sin\beta \\
t_{12} &= \cos\psi\cos\beta \\
t_{13} &= \sin\psi\sin\theta - \cos\psi\cos\theta\sin\beta \\
t_{21} &= -\cos\psi\cos\theta + \mathrm{c}\sin\psi\sin\theta\sin\beta \\
t_{22} &= \sin\psi\cos\beta \\
t_{23} &= -\cos\psi\sin\theta - \sin\psi\cos\theta\sin\beta \\
t_{31} &= -\sin\theta\cos\beta \\
t_{32} &= \sin\beta \\
t_{33} &= \cos\theta\cos\beta
\end{aligned} \tag{2.28}$$

In this study, Fourier series which approximates the blade motion were truncated at the first harmonic for rigid blade motion. Figure 2.2 shows the resulting flapping and pitching motion of the blade separately and Figure 2.3 shows the combined (pitch and flap) blade motion.

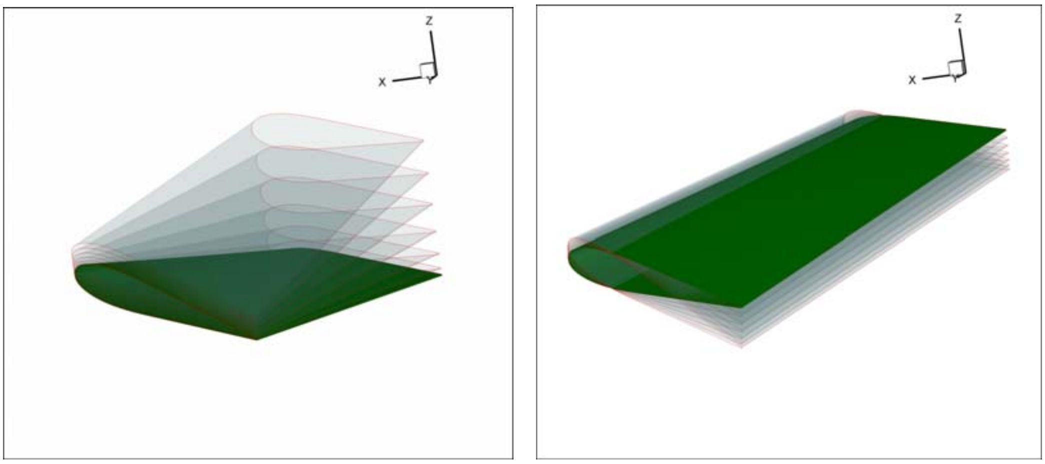

**Figure 2.2:** Flapping (left) and pitching (right) motion of the AH-1G rotor blade

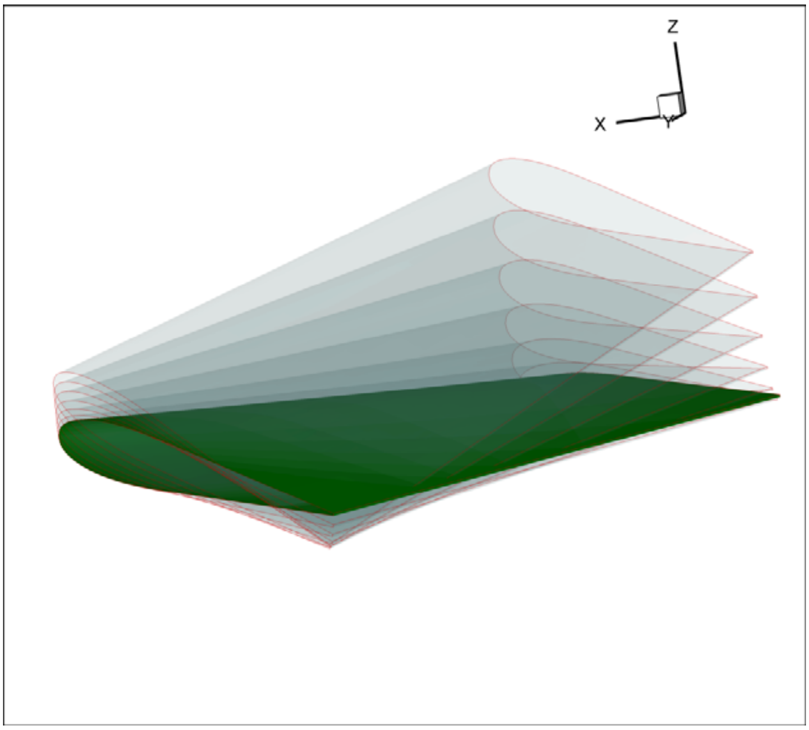

**Figure 2.3:** Combined flapping and pitching motion of the AH-1G rotor blade

# 3 INITIAL AND BOUNDARY CONDITIONS

## 3.1 Hover Details

Boundary conditions applied for the hovering rotor case are shown in Figure 3.1.

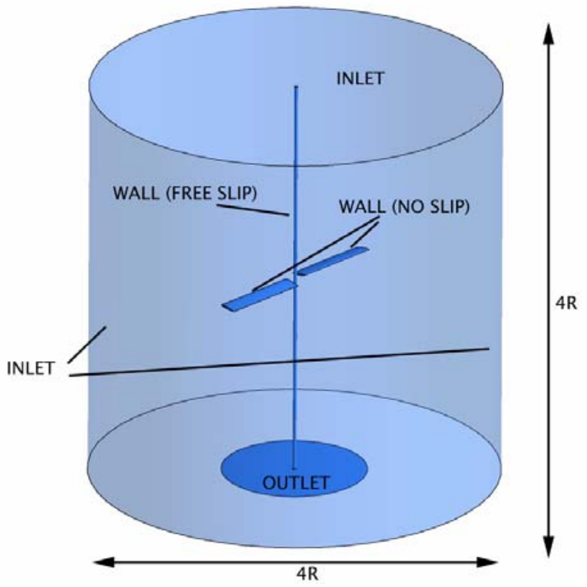

**Figure 3.1**: Boundary conditions for hover case

The usual boundary condition for an isolated hovering rotor is to assume that outside the computational cylinder, the velocity is equal to the free stream velocity. This means that the fluid merely recirculates within the computational domain, but in fact the rotor draws fluid into the rotor-disk from outside the domain. To overcome this inconsistency Srinivasan et. al developed a boundary condition that accounts for the mass flow. Details of this boundary condition are given in section 2.4. This study uses the “hover boundary condition” for modeling the farfield conditions of an isolated hovering rotor. User defined expressions of CFX software were used to calculate the velocities at the boundary faces. This velocity is pointing toward the hub of the rotor blade at all boundary locations as can be seen in Figure 3.2. Static pressure and temperature values were imposed at the outflow boundary. On the blade surfaces no-slip wall boundary condition was applied. Free-slip wall boundary condition was used on the hub surface. Ideal gas law was chosen to define the density. Reference pressure was chosen as 1 atm. Reference temperature is chosen as 288K.

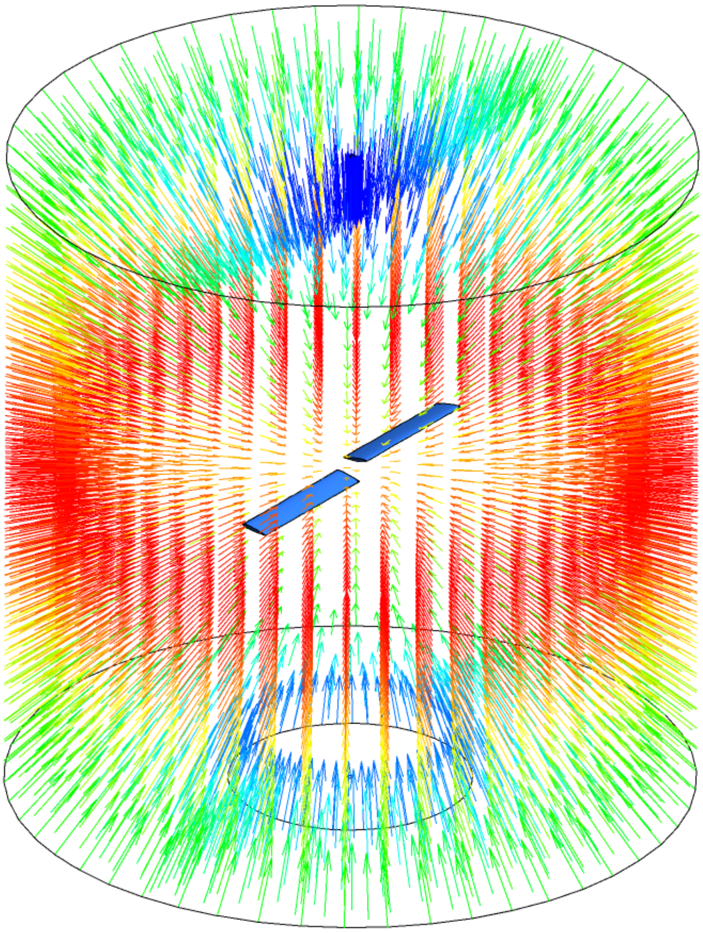

**Figure 3.2:** Velocity vectors at the inlet boundaries

## 3.2 Forward Flight Details

Boundary conditions applied for the forward flight case are shown in Figure 3.3.

Since the assumption of so called hover boundary conditions is no longer valid in forward flight conditions, a much bigger computational domain was chosen and farfield conditions for inlet and outlet were applied directly. Inlet region is shown with green and the outlet region is shown with blue in Figure 3.3. Forward flight velocity taken from the flight test data (42.1844 m/s) was applied at inlet boundary. Static pressure and temperature values were imposed at the outlet boundary. A domain interface was defined between the inner rotating cylindrical domain and stationary outer domain.

On the blade surfaces no-slip wall boundary condition was applied. Free-slip wall boundary condition was used on the hub surfaces. Ideal gas law was chosen to define the density. Reference pressure was chosen as 1 atm. Reference temperature is chosen as 288K.

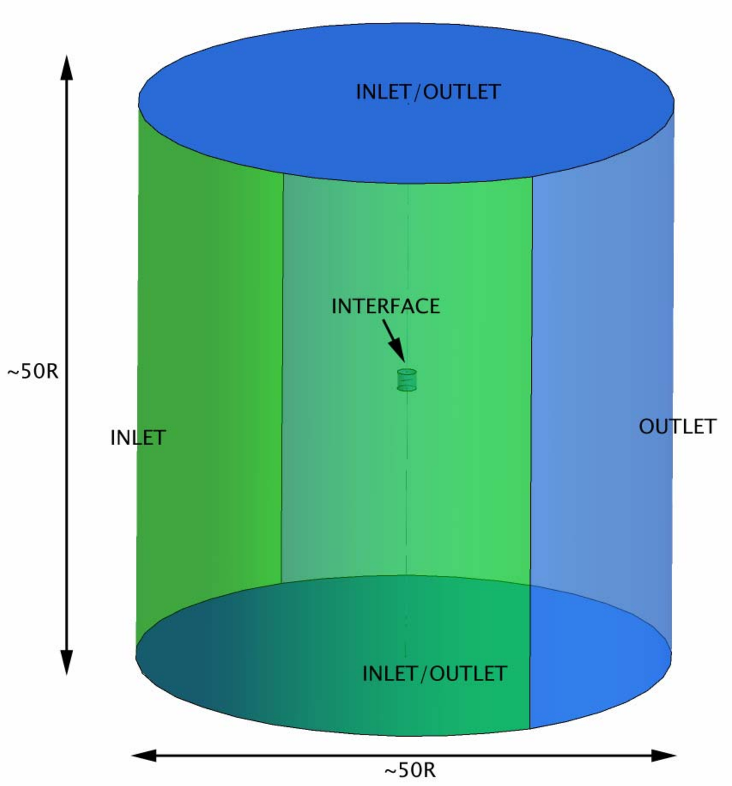

**Figure 3.3:** Boundary conditions for the forward flight case

# 4 MODELING AND GRID INFORMATION

Steady and unsteady flowfields of helicopter rotors in hover and forward flight were analyzed. First, Caradonna&Tung rotor was analyzed at hover conditions with no dynamic blade motion. Having validated the methodology, AH-1G rotor was analyzed in forward flight conditions. Both rotors are two-bladed. Rotation of the blades was modeled using a rotating frame of reference. The flap and pitch motion of the blades' in forward flight are prescribed using the blades' first harmonics measured in the flight tests and the grid was allowed to move accordingly with the pitch and flap motion of the blades. Structured - unstructured mixed grids were generated for both rotors using commercially available grid generation software.

## 4.1 Caradonna-Tung Rotor

The first rotor, which was analyzed in hover conditions for the purpose of validation of the methodology, was the Caradonna-Tung rotor. Caradonna and Tung have carried out experimental and analytical study of this rotor in hover. The rotor consists of two untwisted and untapered planform of NACA0012 profiled blades. A sketch of rotor system can be seen in

Figure **4.1**. Properties of the blades are given in Table 4.1. Calculations were performed for three different tip Mach numbers (Mt= 0.439, 0.727 and 0.877) with the same pitch angle of $\Theta^{o}=8^{o}$.

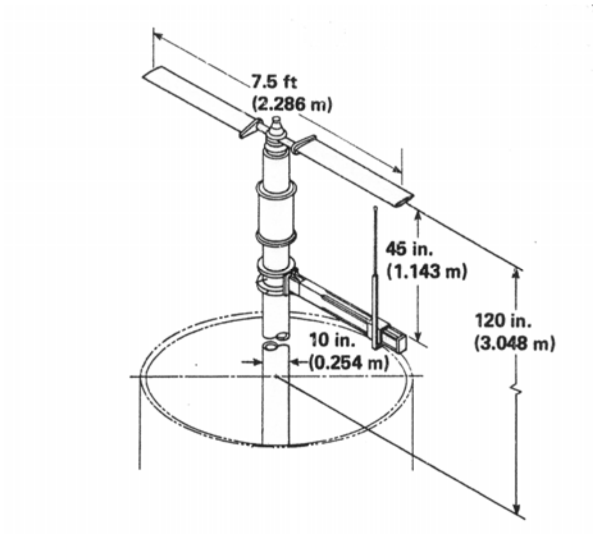

**Figure 4.1:** Caradonna & Tung rotor [16].

**Table 4.1:** Properties of the Caradonna & Tung Rotor

| | |
|---|---|
| Radius, R | 198 mm |
| Chord, c | 33 mm |
| Root cutout, $r_o$ | 0.6c |
| Twist, $\Theta_{tw}$ | $0^0$ |
| Solidity | 0.1 |
| Tip Chord, $c_t$ | 33 mm |
| Root Chord | 33 mm |
| Taper ratio, $\tau$ | - |
| Break point, $r_b$ | - |

The diameter and height of the computational domain size was chosen as 4R where R is the rotor radius. The whole rotor system with two blades was modeled instead of modeling one blade and utilizing periodic boundary conditions. The reason for this is that the hovering rotor calculations were made for verifying the methodology for the forward flight analyses and in the forward flight analyses, the whole rotor system needs to modeled as the flowfield is no longer steady and periodic.

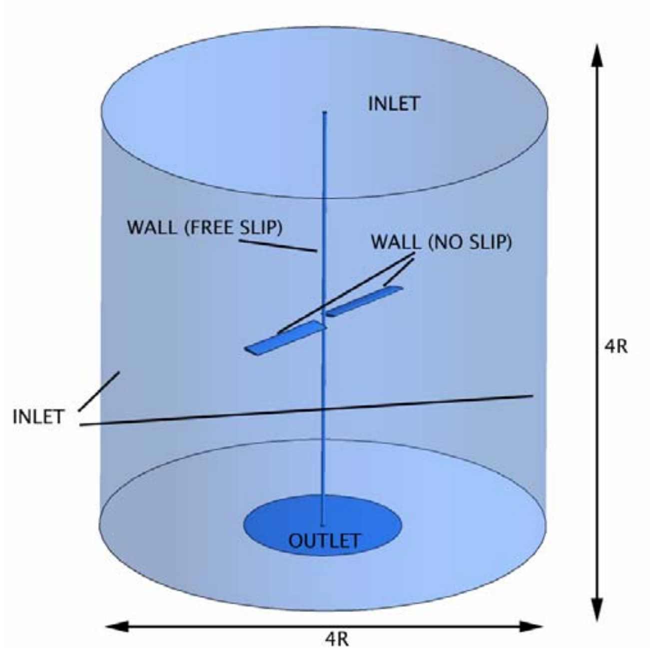

**Figure 4.2:** Computational domain for the hover case

Structured grids, generated by hyperbolic extrusion, consisting entirely of hexahedral cells were used near the rotor blade. For the remaining parts of the computational domain, unstructured grids composed of tetrahedral, pyramid, and prism cells were used. Large hexahedral cells were used in transition areas between the structured and unstructured parts of the grid. Resulting grid has a total of 1.3 million volume elements.

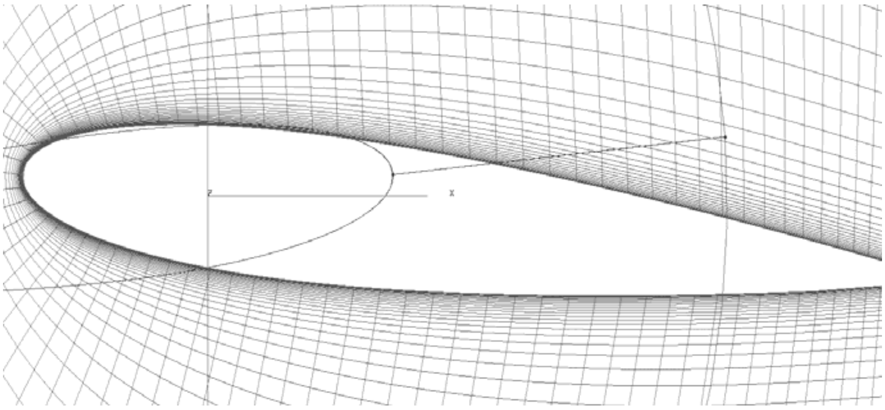

**Figure 4.3:** Close view of the grid around the Caradonna & Tung blade

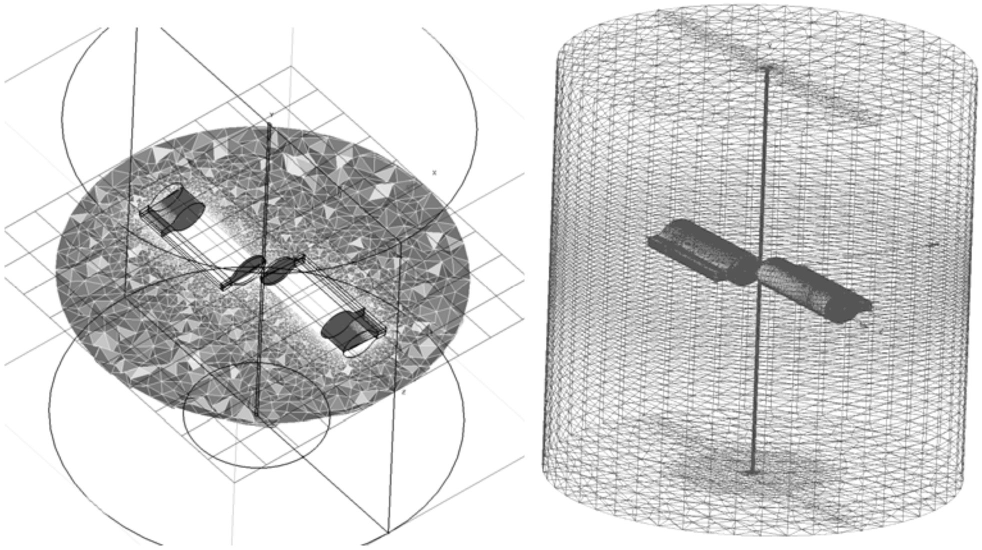

**Figure 4.4:** Views of the computational grid around the Caradonna & Tung rotor

## 4.2 AH-1G Rotor

The second rotor, which was analyzed in forward flight conditions, was the AH-1G rotor and it was tested at NASA Ames Research Center as a part of an operational loads survey program [17]. The AH-1G rotor blade uses an Operational Loads Survey (OLS) symmetrical airfoil section and has an aspect ratio of 9.8. The rotor is a two-bladed rectangular planform teetering configuration with a radius of 6.7056 m. Root cutout is at 0.15R. It has a linear twist of $-10^0$ from root to tip. The case chosen for validation is at an advance ratio of 0.19, $M_t$=0.65 and an overall thrust coefficient of 0.00464. These conditions correspond to a forward speed of 42.1844 m/s at a rotation rate of 316rpm.

The first blade harmonics measured in the flight test is given in Table 4.2.

**Table 4.2**: First blade harmonics measured in the flight test

| $\theta_0$ | $\theta_0$ | $\theta_0$ | $\beta_{1s}$ | $\beta_{1c}$ |
|---|---|---|---|---|
| 6.0 | -5.5 | 1.7 | -0.15 | 2.13 |

These values are not trimmed values. In order to match the measured thrust and eliminate the rolling and pitching moments, manually trimmed values of Sankar & Yang [4] was used. These values are given in Table 4.3.

**Table 4.3**: Manually trimmed first blade harmonics

| $\theta_0$ | $\theta_0$ | $\theta_0$ | $\beta_{1s}$ | $\beta_{1c}$ |
|---|---|---|---|---|
| 8.0 | -6.5 | 2.5 | -0.15 | 2.13 |

Rigid blade motion was assumed and the blade motion is modeled using mesh deformation capabilities of CFX. User expressions, based on the formulation of blade motion explained in 2.6 were created and prescribed at the boundaries of the blades.

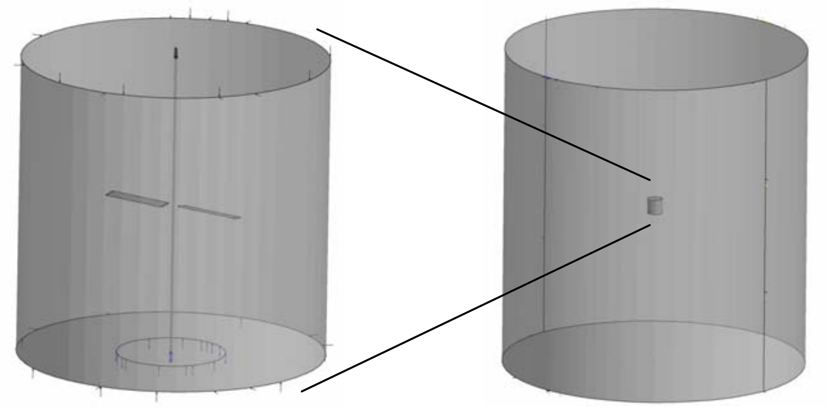

**Figure 4.5**: Forward flight computational domain placement

The computational domain consists of two cylindrical domains. In the inner cylinder, Navier-Stokes equations are solved in a rotating reference frame (

Figure **4.5**). The outer cylinder is stationary. Transition between stationary and rotating reference frames are handled by creating domain interfaces between the surfaces. The diameter and height of the outer computational domain was chosen as 50R where R is the rotor radius.

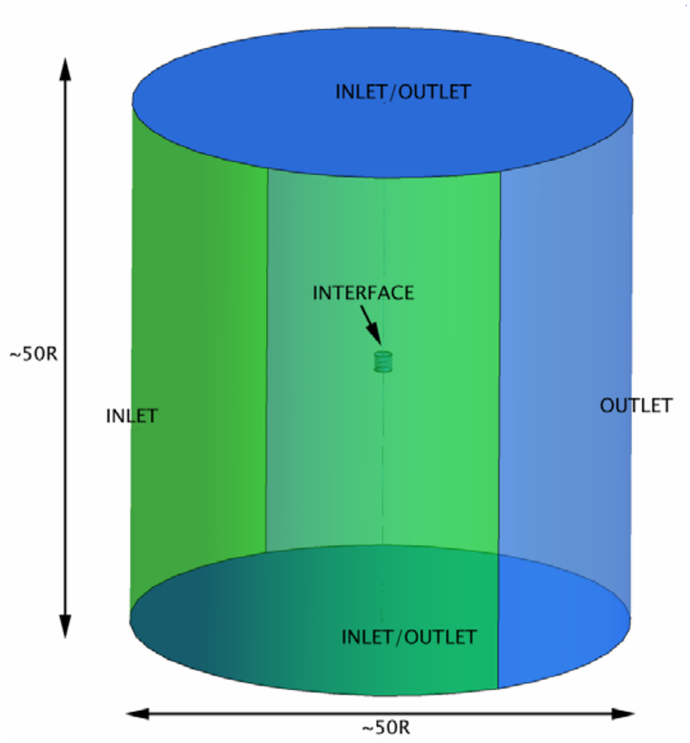

**Figure 4.6:** Computational domain for the forward flight case

Structured grids, generated by hyperbolic extrusion, consisting entirely of hexahedral cells were used near the rotor blade. For the remaining parts of the inner computational domain, unstructured grids composed of tetrahedral, pyramid, and prism cells were used. Large hexahedral cells were used in transition areas between the structured and unstructured parts of the grid. Resulting inner cylindrical domain has a total of 1.1 million volume elements. The outer cylindrical grid is structured and consists entirely of hexahedral cells.

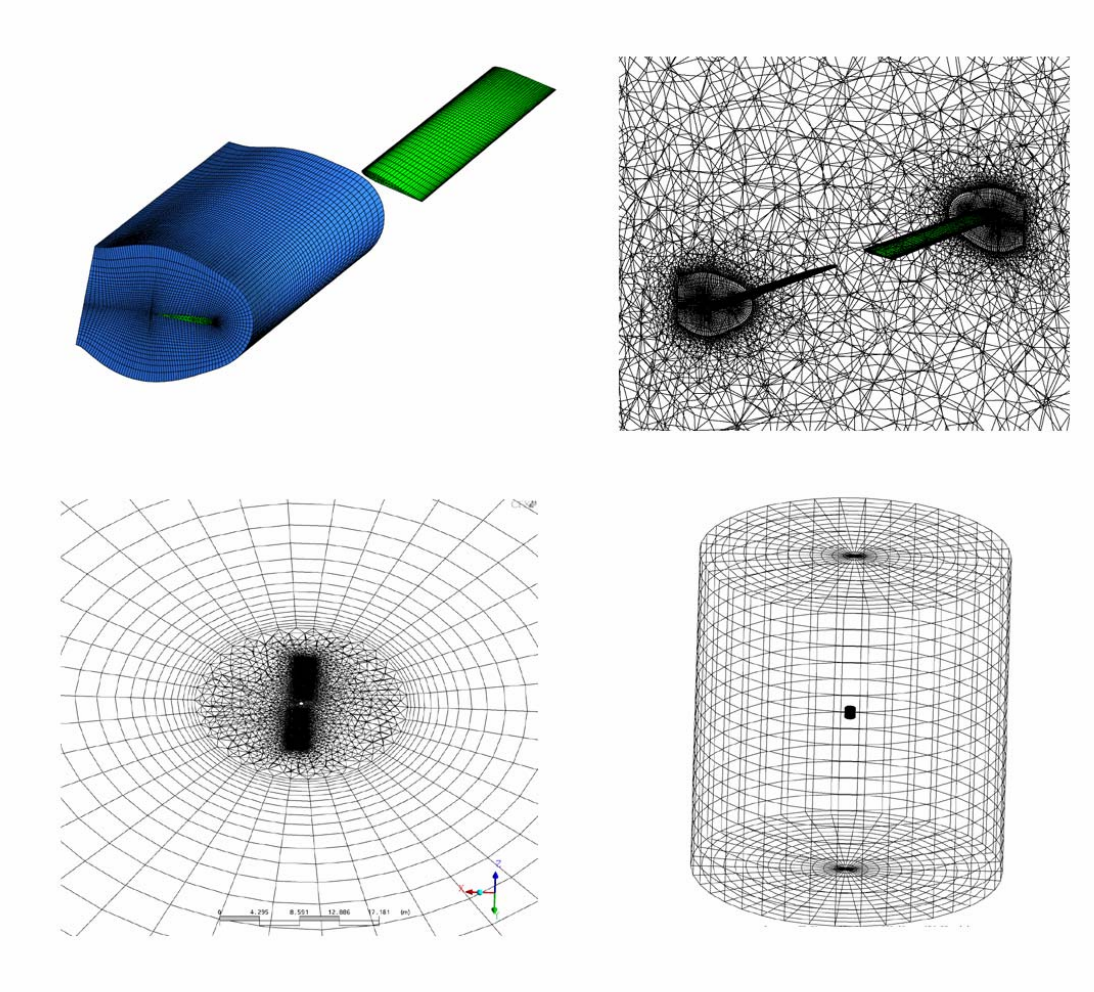

**Figure 4.7:** Various views of the computational grid around the AH-1G rotor

# 5 RESULTS AND DISCUSSION

The flowfield around the helicopter rotors in hover and forward flight conditions were investigated. Hover flight conditions for an isolated rigid rotor was analyzed for assessing the capabilities of the CFX solver and to form a basis for forward flight analyses. The computations were carried out for various flow conditions with different tip Mach numbers and collective pitch settings and the results were compared with the experimental data of Caradonna & Tung [16]. After the hover analyses, AH-1G rotor [17] was analyzed in forward flight conditions and results were compared with flight test data [17] and numerical studies of Yang & Sankar [4].

## 5.1 Caradonna-Tung Rotor

Caradonna & Tung rotor was analyzed in hover conditions given in section 4.1. Results are presented at half of the blade (r/R=50%) and near the blade tip (r/R=96%). An analysis took about 3 days with 8 CPUs on a SGI Altix 3000 system.

There is a good agreement in Mtip=0.439 case, both at r/R=%50 (Figure 5.1) and r/R=%96 (Figure 5.2) stations except a slight overprediction at the upper blade surface.

Figure 5.3 and Figure 5.4 shows the pressure coefficient distributions for Mt=0.727 case for r/R=%50 and r/R=%96 case respectively. At the r/R=%50 station there's an underprediction both at the lower and upper blade surface. At r/R=%96 station, underprediciton at the lower surface is smaller but similar to the r/R=%50 station's results at the upper surface. The results can be said to be in a fairly good agreement with the experimental data.

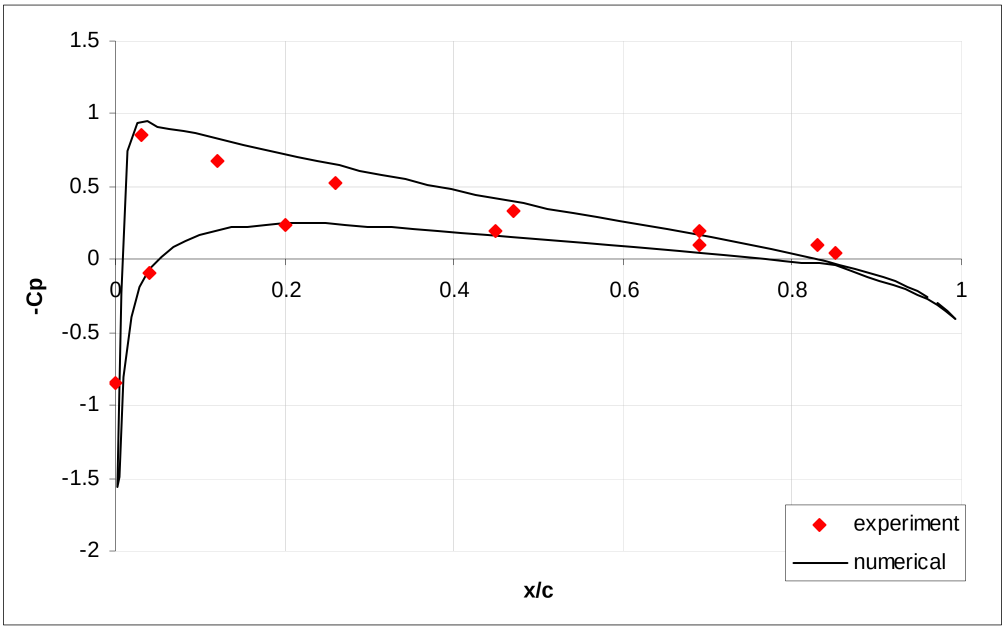

**Figure 5.1:** Comparisons of the experimental pressure coefficient distributions with the present study for the Caradonna&Tung rotor [r/R=50%, Mt=0.439, ϴ°=8°].

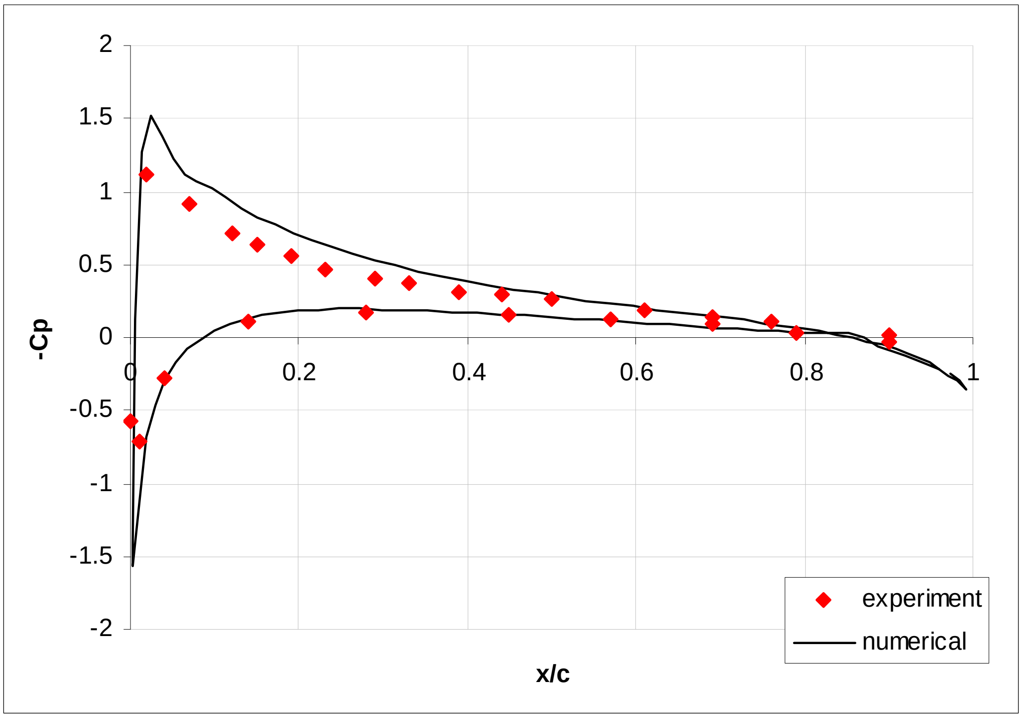

**Figure 5.2:** Comparisons of the experimental pressure coefficient distributions with the present study for the Caradonna&Tung rotor [ r/R=96%, Mt=0.439,ϴ°=8°].

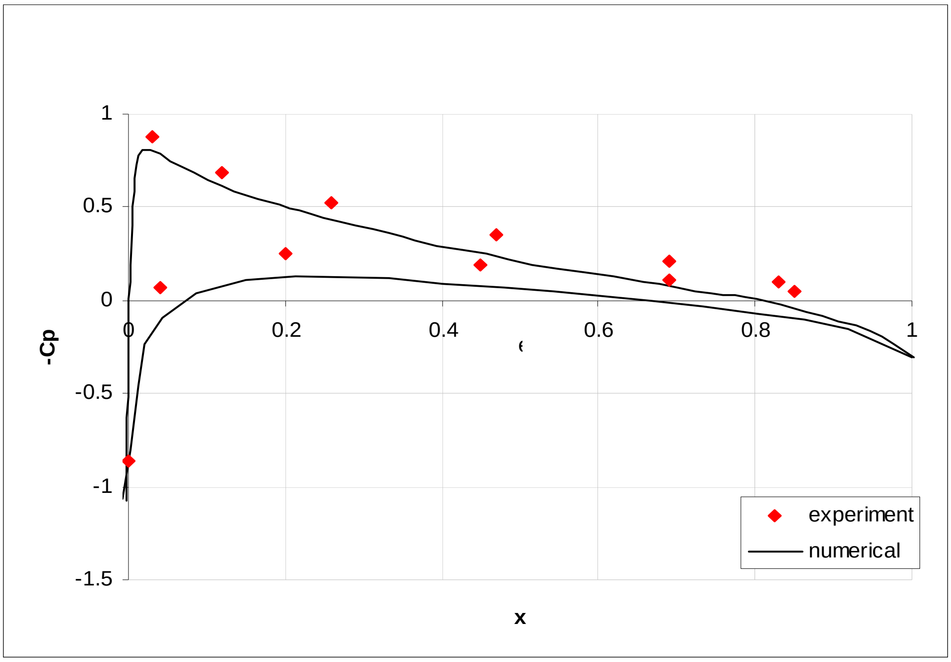

**Figure 5.3:** Comparisons of the experimental pressure coeffient distributions with the present study for the Caradonna&Tung rotor [ r/R=50%, Mt=0.727, $\Theta^o=8^o$].

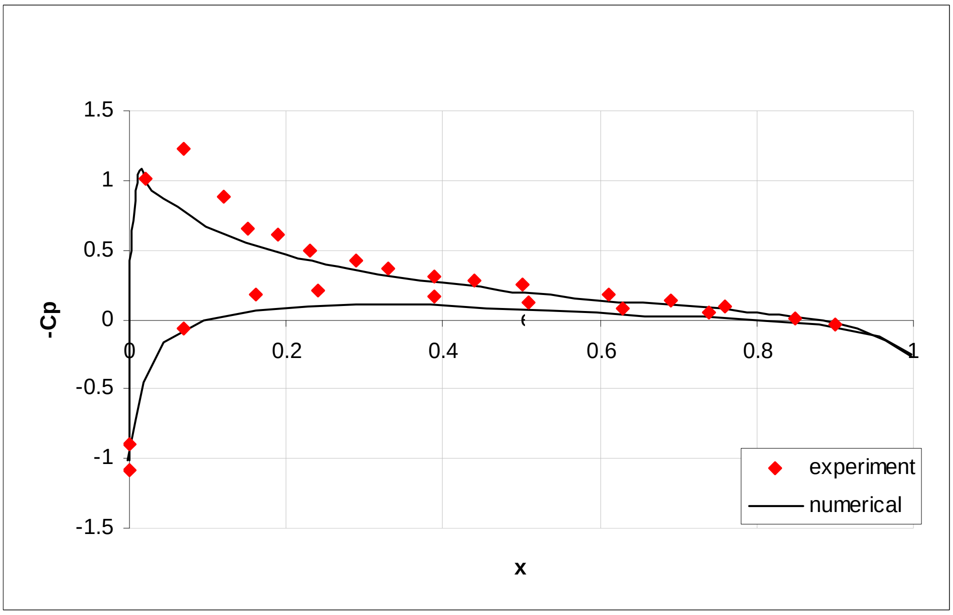

**Figure 5.4:** Comparisons of the experimental pressure coefficient distributions with the present study for the Caradonna&Tung rotor [r/R=96%, Mt=0.727, $\Theta^o=8^o$].

For the $M_t$=0.877 case, at r/R=%50 station lower surface (Figure 5.5) results is close to the experimental results but there's a big overprediction at the upper surface. At the r/R=%96 station, experimental results indicate a shock at upper surface (Figure

5.6). Numerical results capture a shock at the upper surface but the agreement is very poor.

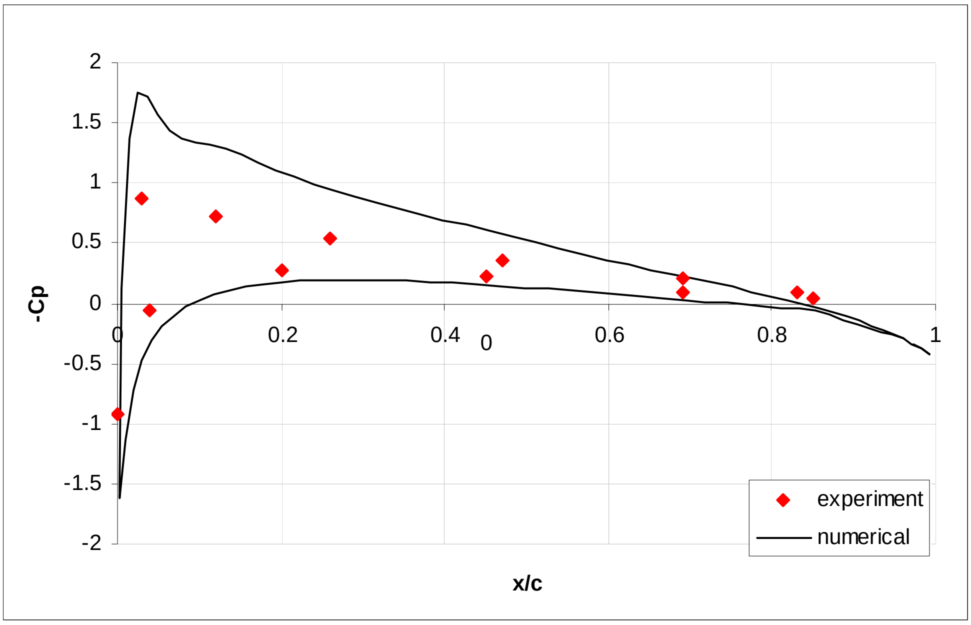

**Figure 5.5:** Comparisons of the experimental pressure coefficient distributions with the present study for the Caradonna&Tung rotor [r/R=50%, Mt=0.877,$\Theta_0$=$8_0$].

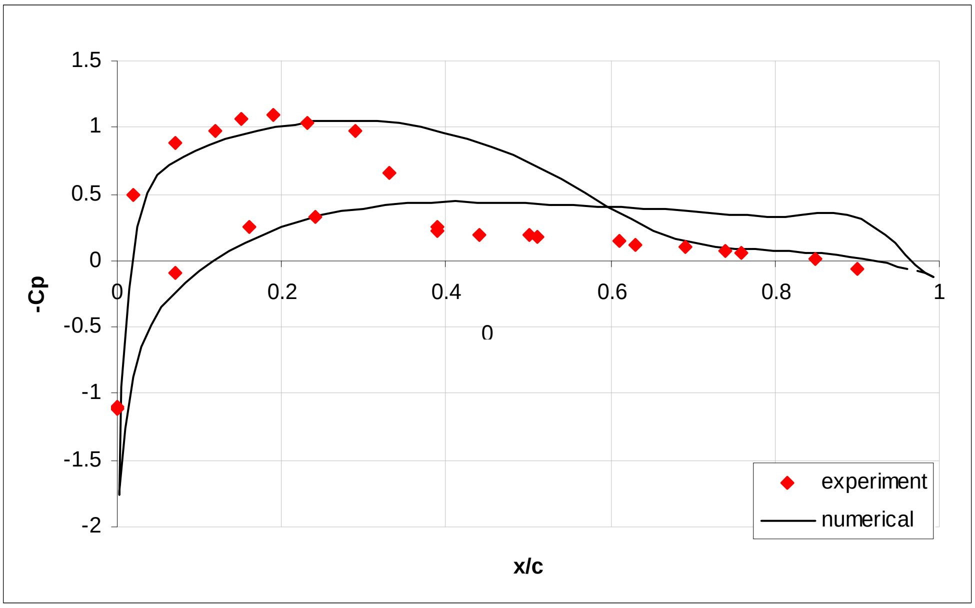

**Figure 5.6:** Comparisons of the experimental pressure coefficient distributions with the present study for the Caradonna&Tung rotor [r/R=96%, Mt=0.877, $\Theta^o$=$8^o$].

Figure 5.7 shows a velocity vector plot of the flow field. The tip vortices can be seen clearly. Figure 5.8 shows a closer view of the tip vortex.

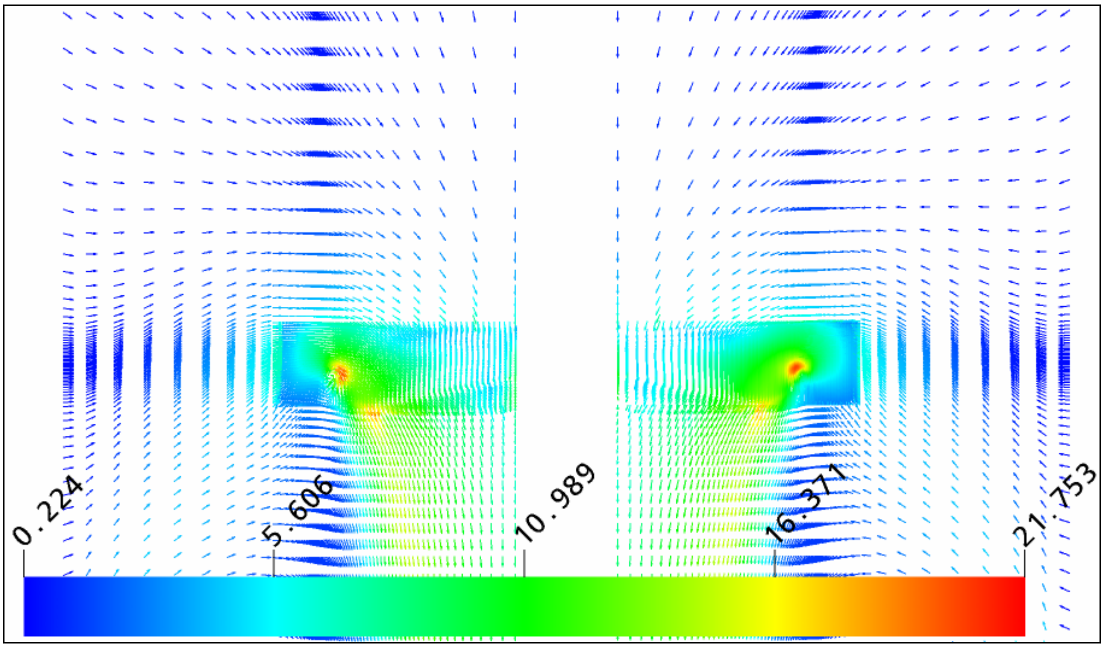

Figure 5.7: Velocity vectors of the flowfield.

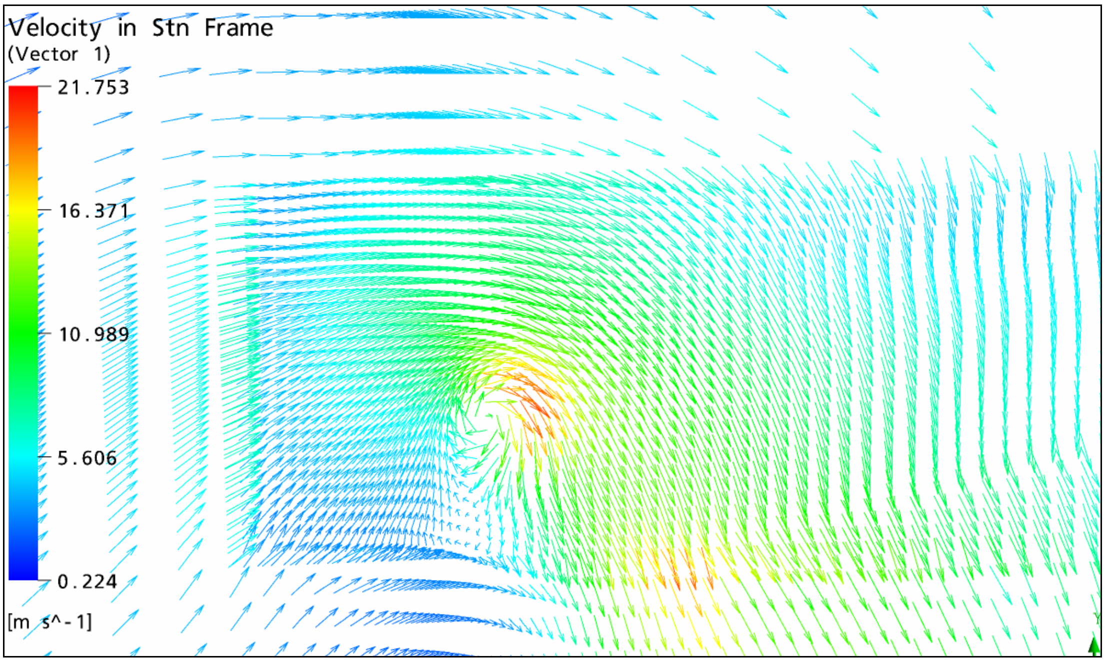

**Figure 5.8:** Closer view of the tip vortex.

### 5.2 AH-1G Rotor

AH-1G rotor was analyzed in forward flight conditions given in section 4.2. Results are presented at r/R=60% and r/R=91% stations.

Analysis times for forward flight computations were very long in comparison with hover analyses. It took about three weeks for three revolutions of the rotor with 8 CPUs on an SGI Altix 3000 system. The main reason for this can be the mesh deformation calculations and additional computational load caused by the interpolation calculations for the domain interfaces.

Forward flight analyses were first made with flapping only blades. The pitching motion of the blades was added to the model later. Results are presented both for flapping only motion and flapping and pitching motion of the blades.

Figure 5.9 shows the pressure coefficient distributions at the r/R=60% station at $\psi = 30^0$. Flap-only and flap-pitch combined results agree relatively well with the experimental and numerical data.

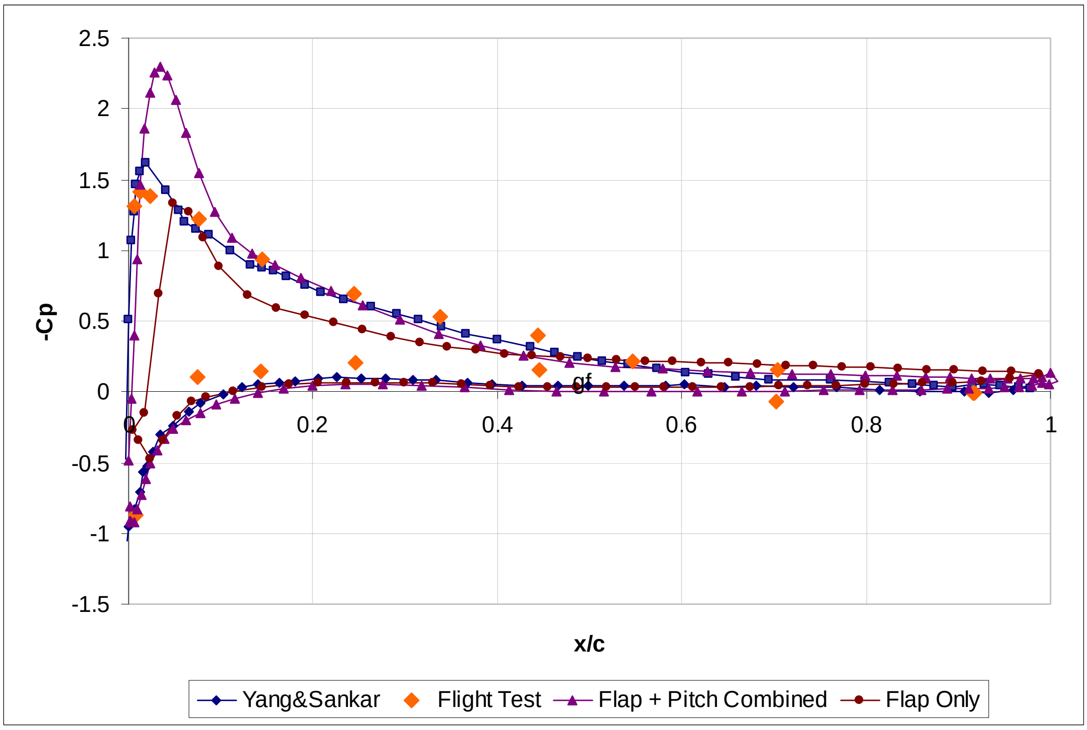

**Figure 5.9:** Comparisons of the pressure coefficient distributions with the present study for the AH-1G rotor (r/R=60%, $\psi = 30^0$)

Figure 5.10 shows the pressure coefficient distributions at the r/R=60% station at $\psi = 180^0$. Pressure coefficients at the upper surface agree with the experimental data better than Yang&Sankar. At the lower surface, both flap-only and flap-pitch combined results overpredict the pressure coefficient.

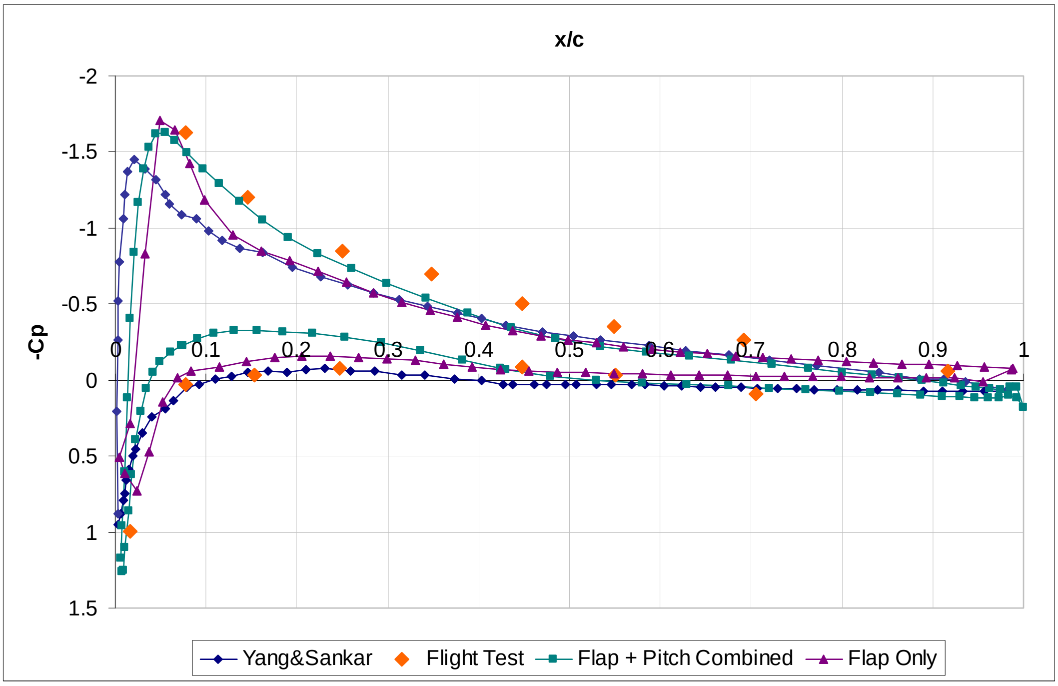

**Figure 5.10:** Comparisons of the pressure coefficient distributions with the present study for the AH-1G rotor (r/R=60%, $\psi = 180^0$)

Figure 5.11 shows the pressure coefficient distributions at the r/R=91% station at $\psi = 90^0$. Agreement with experimental and numerical results is very poor at the upper blade surface both for flap-only and flap-pitch combined results. A relatively good agreement at the lower surface can be said to exist for the flap-pitch combined results.

Figure 5.12 shows the pressure coefficient distributions at the r/R=91% station at $\psi = 105^0$. Results look similar to the $\psi = 90^0$ position and agreement is very poor.

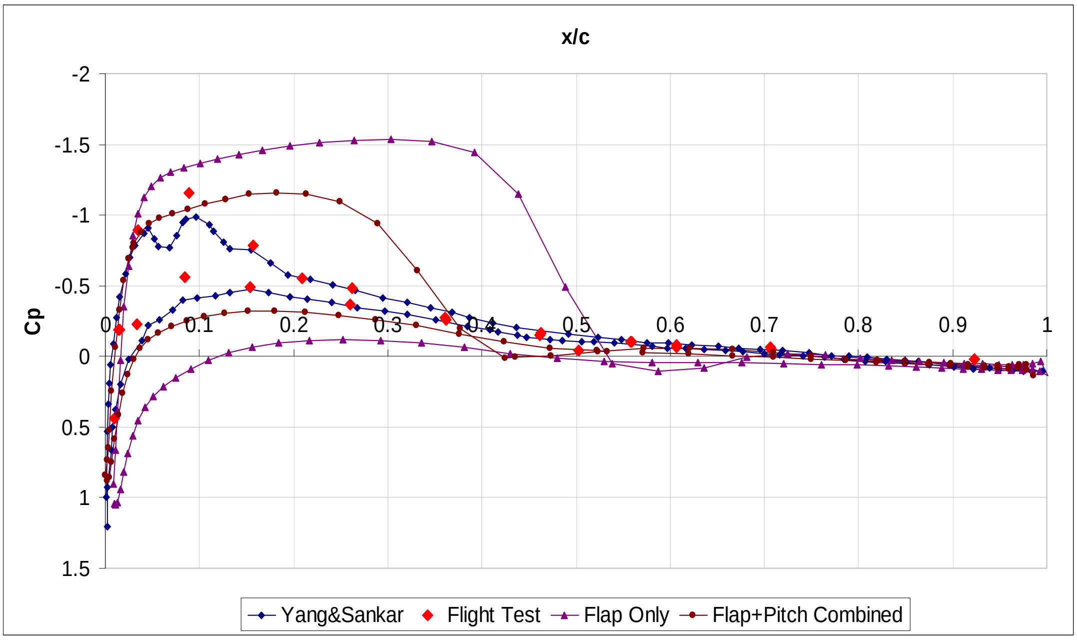

**Figure 5.11:** Comparisons of the pressure coefficient distributions with the present study for the AH-1G rotor (r/R=91%, $\psi = 90^0$)

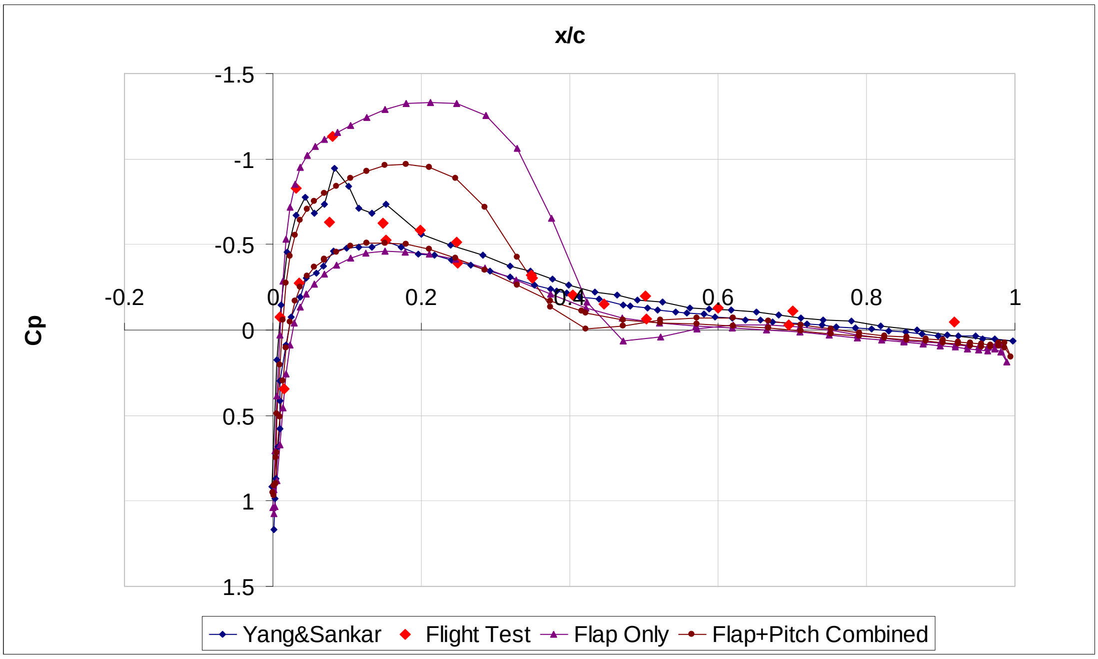

**Figure 5.12:** Comparisons of the pressure coefficient distributions with the present study for the AH-1G rotor (r/R=91%, $\psi = 105^0$)

Evolution of a tip vortex and the interaction with the following blade is shown in Figure 5.13.

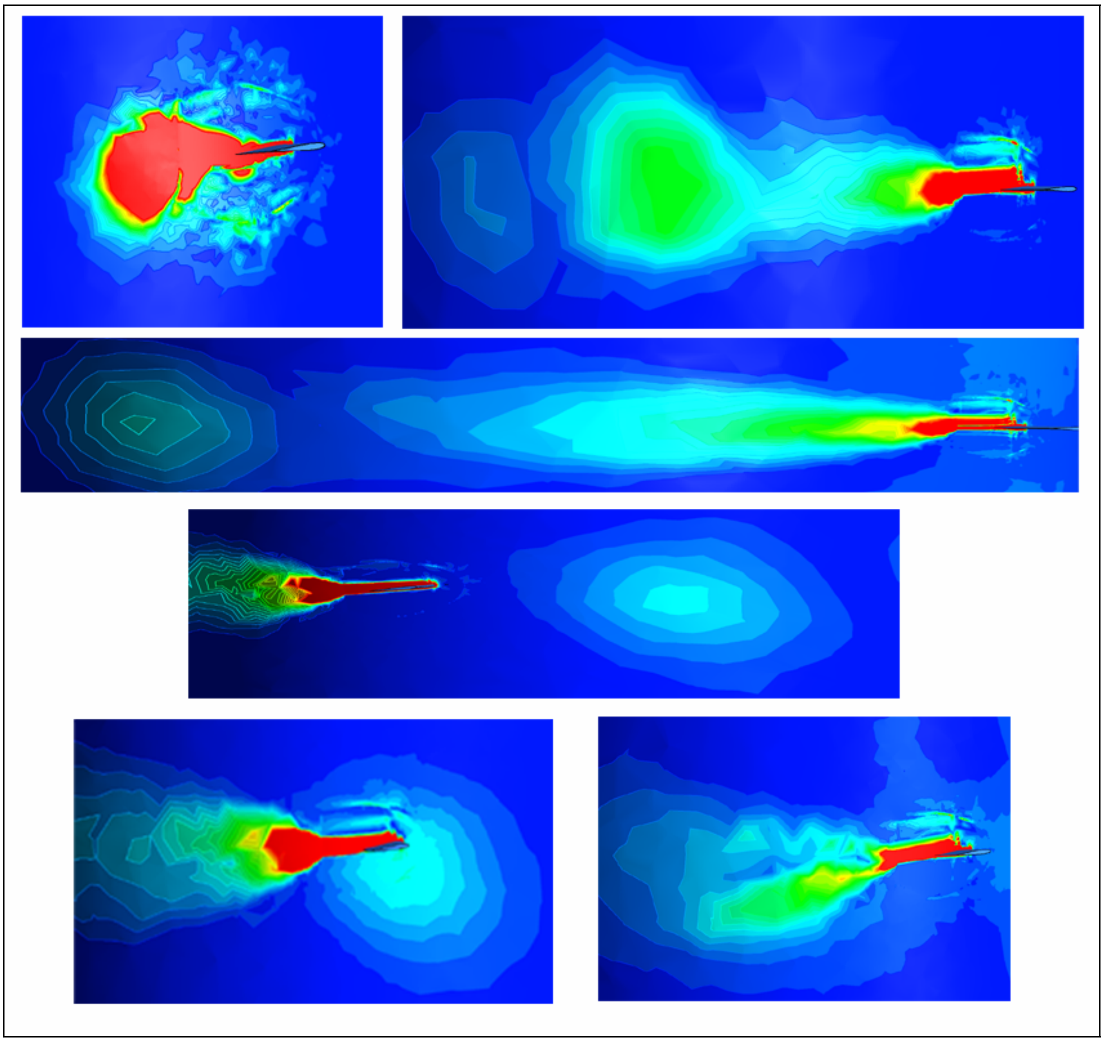

**Figure 5.13:** Tip vortex formation and interaction with the following blade.

# 6 CONCLUSIONS

In this study, flow field around hovering and forward flying rotors was analyzed using commercial CFD software (ANSYS CFX 10). Mesh generation was also made with commercial grid generation software Pointwise GRIDGEN.

First an isolated hovering rotor is analyzed and results are compared with experimental data. The overall agreement is good except the high tip speed case where there are shocks near the blade tip. It is observed that discrepancy between the experimental and numerical results increases with the increase of the tip Mach number.

Second part of this study was the analysis of a rotor in forward flight conditions. A relatively simple rotor was chosen and analyzed for comparison against flight test data and another numerical study. It may be said that the present results agree with experimental and numerical data at the inner sections of the blade. Near the tip of the blade, results suggest that there exists a shock forming on the blade and agreement is very poor. This looks similar to the shock case of hovering rotor and needs to be investigated further. Analysis time for the forward flight analyses was about 3 weeks for 3 revolutions with 8 CPUs. The main reason for this may be the mesh deformation calculations and domain interface interpolation calculations. This long runtime prevents the current method from being used for practical applications.

Generation of the grids was also a very time consuming task and many trials needed to be done before successfully generating a grid. An automated grid generator for helicopter rotor analyses would be a very valuable tool and should be developed in the near future.

An attempt to improve the results by refinement of the inner mesh only, was not successful. It is understood that the whole computational domain grid (both inner and outer cylindrical domains) should be refined for a successful analysis, which requires even longer run times.

## REFERENCES

[1] **Leishman J. Gordon,** 2000. Principles of Helicopter Aerodynamics, Cambridge University Press, United Kingdom

[2] **Conlisk A.T**., 1997. Modern Helicopter Aerodynamics, *Annual Review of Fluid Mechanics*, **29**, 515-567

[3] **Caradonna, F.X. and Tung, C.**, 1992. The application of CFD to rotary wing aircraft, NASA TM-102803

[4] **Yang, Z., Sankar, L. N., Smith, M., Bauchau, O**., 2000. Recent improvements to a hybrid method for rotors in forward flight, AIAA paper

[5] **Egolf, T. A., Sparks, S.P.**, 1986. A full potential rotor analysis with wake influence using an inner-outer domain technique, *Proc. Annu. Forum Am. Hel. Soc.*, **42nd**, 997-1011

[6] **Strawn, R.C., Caradonna, F.X**., 1987. Conservative full potential method for unsteady transonic rotor flows, *AIAA Journal*, **25(2)**, 193-198

[7] **Steinhoff, J., Ramachandran, K.,** 1990. Free wake analysis of compressible rotor flows, *AIAA Journal*, **28(3)**, 426-431

[8] **Ramachandran, K., Schlechtriem, S., Caradonna, F.X., Steinhoff, J.,** 1993. The application of vorticity embedding to the computation of advancing rotor flows., *Annu. Forum Am. Hel. Soc.*, **49th**, 571-584

[9] **Wake, B. E., Sankar, L.N.,** 1989. Solutions of the Navier-Stokes equations for the flow about a rotor blade, *J. Am. Hel. Soc.*, **34**, no 2:13-23.

[10] **Srinivasan, G.R., Raghavan, V., Duque E.P.N., and McCroskey, W.J.**, 1993. Flowfield of a Lifting Rotor in Hover by Navier-Stokes Method, *Journal of the American Helicopter Society*, **38**, 1-11.

[11] **Srinivasan, G.R., Baeder, J.D.,** 1993. TURNS: A free-wake Euler-Navier-Stokes numerical method for helicopter rotors, *AIAA Journal*, **31(5)**, 959-962

[12] **Ahmad, J., Duque, E.**, 1996. Helicopter Rotor Blade Computation in Unsteady Flows Using Moving Overset Grids, *Journal of Aircraft*, **Vol.33** No: 1, pp.54-60.

[13] **Steijl, R., Barakos, G., Badcock, K.**, 2005. A framework for CFD analysis of helicopter rotors in hover and forward flight, *Int. Journal for Numerical Methods in Fluids*, **51**, 819-847

[14] **Pomin, H., and Wagner, S**., 2004. Aeroelastic analysis of helicopter rotor blades on deformable chimera grids, *Journal of Aircraft,* **Vol. 41**, No. 3

[15] Ansys CFX 10.0 Solver Theory Manual, 2005. Ansys Inc.

[16] **Caradonna, F.X. and Tung, C.**, 1981. Experimental Analytical Studies of a Model Helicopter Rotor in Hover, NASA TM-81232

[17] **Cross, J. F. And Watts, M. E.**, 1988. Tip aerodynamics and acoustics test, NASA Reference Publication 1179

[18] **Menter, F.R.,** 1994. Two-equation eddy-viscosity turbulence models for engineering applications, *AIAA-Journal.*, **32,** 8

[19] **Q.-J. Zhao et al.**, 2005. Numerical simulations of the unsteady flowfield of helicopter rotors on moving embedded grids, *Aerospace Science and Technology*, **9** 117-124

# APPENDIX A

Below is the user defined expressions for modeling the hover boundary condition in the hovering rotor calculations.

Ct = 0.00461

yaricap = 1.143 [m]

dd = (sqrt(x^2 + y^2 + z^2) )

vtip = 245.37 [ m s^-1 ]

Vmag = vtip*sqrt(Ct/32) * ((yaricap/dd)^2)

bcU = -(Vmag*(x/dd))

bcV = -Vmag*(y/dd)

bcW = -Vmag*(z/dd)

## APPENDIX B

User defined expressions for modeling the flapping and pitching blade motion in the forward flight calculations are given below.

```
deg2rad = 0.01745329251994

dt = 5.274e-4 [s]

dtheta = (dtstep/5.274e-4 [s])*atstep

pala1azimuth = 180

pala1azimuthactual = (pala1azimuth+dtheta)*deg2rad

pala1beta1s = -0.15*deg2rad

pala1beta1c = 2.13*deg2rad

pala1beta1actual = pala1beta1c*cos(pala1azimuthactual)+\
pala1beta1s*sin(pala1azimuthactual)

pala1beta1 = -pala1beta1actual

pala1theta1s = -6.5*deg2rad

pala1theta1c = 2.5*deg2rad

pala1theta1actual = pala1theta1c*cos(pala1azimuthactual)+\

pala1theta1s*sin(pala1azimuthactual)

pala1theta1 = -pala1theta1actual

pala1t21 = -cos(pala1theta1)*sin(0)

pala1t31 = sin(pala1theta1)

pala1t11 = cos(pala1theta1)*cos(0)

pala1newx = (x*pala1t11+y*pala1t21+z*pala1t31)-x

pala1t12 = cos(pala1beta1)*sin(0)+sin(pala1beta1)* \
```

```
sin(pala1theta1)*cos(0)

pala1t32 = -cos(pala1theta1)*sin(pala1beta1)

pala1t22 = cos(pala1beta1)*cos(0)- \

sin(pala1beta1)*sin(pala1theta1)*sin(0)

pala1newy = (x*pala1t12+y*pala1t22+z*pala1t32)-y

pala1t13 = sin(0)*sin(pala1beta1)-cos(pala1beta1)* \

sin(pala1theta1)*cos(0)

pala1t33 = cos(pala1beta1)*cos(pala1theta1)

pala1t23 = cos(0)*sin(pala1beta1)+cos(pala1beta1)* \ sin(pala1theta1)*sin(0)

pala1newz = (x*pala1t13+y*pala1t23+z*pala1t33)-z

pala2azimuth = 0

pala2azimuthactual = (pala2azimuth+dtheta)*deg2rad

pala2beta1s = -0.15*deg2rad

pala2beta1c = 2.13*deg2rad

pala2beta1actual =  pala2beta1c*cos(pala2azimuthactual)+pala2beta1s*
\sin(pala2azimuthactual)

pala2beta1 = pala2beta1actual

pala2theta1c = 2.5*deg2rad

pala2theta1s = -6.5*deg2rad

pala2theta1actual=pala2theta1c*cos(pala2azimuthactual)+ \

pala2theta1s*sin(pala2azimuthactual)

pala2theta1 = pala2theta1actual

pala2t21 = -cos(pala2theta1)*sin(pala2azimuth)

pala2t31 = sin(pala2theta1)

pala2t11 = cos(pala2theta1)*cos(pala2azimuth)

pala2newx = (x*pala2t11+y*pala2t21+z*pala2t31)-x
```

```
pala2t22 = cos(pala2beta1)*cos(pala2azimuth)- \

sin(pala2beta1)*sin(pala2theta1)*sin(pala2azimuth)

pala2t32 = -cos(pala2theta1)*sin(pala2beta1)

pala2t12 = cos(pala2beta1)*sin(pala2azimuth)+sin(pala2beta1)* \

sin(pala2theta1)*cos(pala2azimuth)

pala2newy = (x*pala2t12+y*pala2t22+z*pala2t32)-y

pala2t13 = sin(pala2azimuth)*sin(pala2beta1)- \

cos(pala2beta1)*sin(pala2theta1)*cos(pala2azimuth)

pala2t33 = cos(pala2beta1)*cos(pala2theta1)

pala2t23 = cos(pala2azimuth)*sin(pala2beta1)+cos(pala2beta1)* \
sin(pala2theta1)*sin(pala2azimuth)

pala2newz = (x*pala2t13+y*pala2t23+z*pala2t33)-z
```

## RESUME

Evren ÖNER was born in Lüleburgaz, Turkey in 1978. He graduated from Astronautical Engineering Department of Istanbul Technical University in 2002. He started his graduate education at Advanced Technologies Department of Aerospace Engineering Programme of Istanbul Technical University in 2004. He is currently working as a research engineer at I.T.U. Rotorcraft Center of Excellence (ROTAM).